International Journal of Microwave and Wireless Technologies

cambridge.org/mrf

A fast phase calibration method for a liquid crystal microwave phased array antenna assisted by neural network

Qianying Yan[1], Yanwei Huang[1], Wenzhao Zhang[1], Xin Hou[1], Mengqing Zhang[1], Xiangru Wang[1] and Feng Liang[2]

[1]School of Optoelectronic Science and Engineering, University of Electronic Science and Technology of China, Chengdu, China and [2]School of Physics, University of Electronic Science and Technology of China, Chengdu, China

Research Paper

Cite this article: Yan Q, Huang Y, Zhang W, Hou X, Zhang M, Wang X, Liang F (2024) A fast phase calibration method for a liquid crystal microwave phased array antenna assisted by neural network. *International Journal of Microwave and Wireless Technologies*, 1–10. https://doi.org/10.1017/S175907872400014X

Received: 9 June 2023
Revised: 5 January 2024
Accepted: 5 January 2024

Keywords:
liquid crystal; microwave phased array; neural network; phase calibration

Corresponding author: Xiangru Wang; Email: xiangruwang@uestc.edu.cn

Abstract

Liquid crystal microwave phased arrays (LC-MPAs) are regarded as an ideal approach to realize compact antennas owing to their advantages in cost, size, weight, and power consumption. However, the shortcoming in low radiation deflection efficiency has been one of LC-MPAs' main application limitations. To optimize the steering performance of LC-MPAs, it is essential to model the channel imperfections and compensate for the phase errors. In this paper, a phase error estimation model is built by training a neural network to establish a nonlinear relationship between the near-field phase error and the far-field pattern, hence realizing fast calibration for LC-MPAs within several measured patterns. Simulations and experiments on a 64-channel, two-dimensional planar antenna were conducted to validate this method. The results show that this method offers precise phase error estimations of 3.58° on average, realizes a fast calibration process with several field-measured radiation patterns, and improves the performances of the LC-MPA by approximately 4%–10% in deflection efficiency at different steering angles.

Introduction

Microwave phased arrays (MPAs) have ubiquitous applications in wireless communications due to their performances in precision, speed, and stability [1, 2]. However, traditional MPAs consisting of transmitting and receiving components are costly, bulky, and energy-intensive, limiting their wide applications in commercial markets [3]. In contrast, liquid crystal (LC) MPAs, with advantages in size, weight, power consumption, and monetary cost, have become a topical approach to realizing compact antennas in recent years [4]. LC has been widely used in optical modulators [5–7], yet its application in MPA is still in its infancy. One of the main shortcomings of LC-MPAs is their low deflection efficiency. It is caused by various factors, including manufacturing imperfections, channel crosstalk, and measurement errors [8]. All of these are manifested as phase errors in the near-field phased array (PA) channels, resulting in decreased deflection efficiency in the far-field radiation pattern.

There are two main approaches to MPAs' performance optimization: improving devices' design [9–12] and compensating for phase errors by adjusting the driving voltages applied to each channel through control algorithms. Many control algorithms have been proposed, mainly divided into two categories: iteration methods and noniteration methods. Iteration methods, such as the stochastic parallel gradient descent (SPGD) algorithm [13], the particle swarm optimization [14], and the genetic algorithm [15], use the real-time far-field radiation pattern as an evaluation function to adjust the driving voltages iteratively. However, this approach is impractical for LC antennas since the response of LC phase shifters is relatively slow. It takes minutes to measure a far-field pattern [16], and the time consumption for iteration will be unacceptable. Therefore, noniteration methods, dispensing with the iteration process, and compensating for the phase errors based on the model of the near-field phase aberrations [17] are more viable for LC-MPAs, in which the precision of phase distortions is critical. Nonetheless, the near-field phase errors can be neither directly measured nor mathematically modeled due to their complexity and randomness.

Machine learning provides a promising solution to the model of phase aberrations. The neural networks (NNs) have the ability to extract the nonlinear relations between input and output datasets [18]. By adjusting the weights of nodes in different layers of the NN, a phase estimation model that infers near-field phase error with the given far-field radiation pattern is established, hence calibrating the LC-MPA. Many proposals have been reported

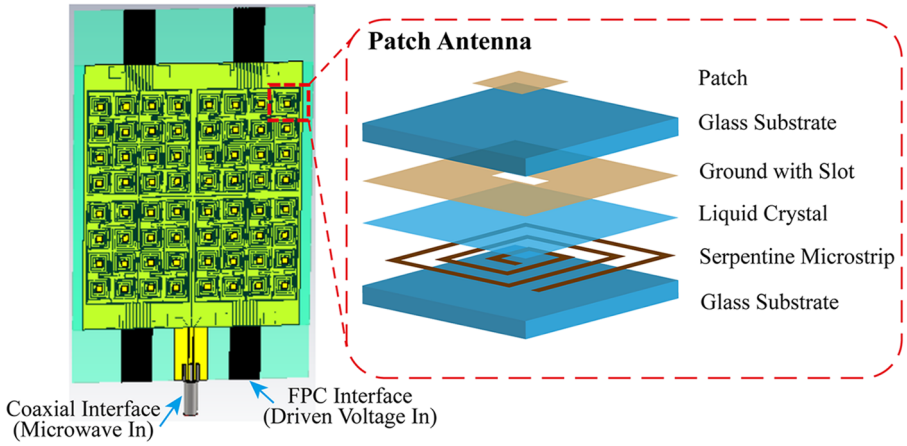

Figure 1. Structure of the LC-MPA antenna.

to optimize the PA using NNs, such as the radial basis function neural network in weather radar [19], the graph neural network in communication systems [20], and the deep neural network in the analysis and beamforming of power patterns [21].

In this paper, a fast phase calibration method is proposed to optimize the steering performance of a 64-channel, two-dimensional planar LC-MPA antenna. A phase error estimation model is built by training an NN to establish a nonlinear relationship between the near-field phase error and the far-field pattern. Simulations show that this model offers precise phase error estimations of 3.58° on average. Numerical simulation and experiments were conducted to verify this method. The results show that the calibration to the near-field phase aberrations is realized with several measured far-field patterns, leading to a considerable increase in the antenna's deflection efficiency and laying a foundation for LC-MPA's in-situ optimization in practical application.

Method

Principle of LC microwave antennas

The LC-MPA used in the following simulations and experiments is shown in Fig. 1, with a detailed structure of its patch antenna, which consists of six layers [22]. The LC layer and the serpentine microstrip combine to be an LC phase shifter. In the default state, the LC permittivity is $\epsilon_{r,\perp}$, and the directors of the nematic LC are perpendicular to the polarization of the microwave field. When a properly driven voltage is applied to the LC, the directors are forced to orient parallel to it. When the driven voltage is higher than the saturated voltage, the permittivity of LC is $\epsilon_{r,\parallel}$. The maximum phase shift of an LC phase shifter is described as follows [23]:

$$\Delta\Phi = \frac{2\pi f}{c_0} L\left(\sqrt{\epsilon_{r,\parallel}} - \sqrt{\epsilon_{r,\perp}}\right), \tag{1}$$

where f is the center frequency, L is the length of the serpentine microstrip, and c_0 is the vacuum speed of the wave.

The microwave signal is transmitted into the antenna through a coaxial interface, and the signal will reach the phase shifter after passing the power distribution network. At the same time, the control voltage drives the antenna through the flexible printed circuit (FPC) interface. The dielectric constant of LC changes in response to the electric field, and therefore, the phase of the transmitted signal alters according to the driven voltage value when passing the LC phase shifter. The microwave signal transmits from the LC phase shifter to the patch on top of the element and then radiates.

Antenna modeling and dataset generation

To obtain the dataset of radiation power patterns and the corresponding phase errors, an LC-MPA simulation model was built, in which a specific range of uniformly selected random errors was applied to each phase shifter element. The simulation model is a uniform 8×8-element rectangular planar array, with a center frequency of 28.6 GHz and the element gap of 0.75 wavelengths, the same as the structure of LC-MPA in Fig. 1. The phase shifter elements in the simulation model are treated as a set of dots.

The simulated antenna model outputs a radiation field pattern when a desired deflection angle is inputted, which is expressed as follows:

$$E(\theta,\phi) = e^{j^*\boldsymbol{\sigma}} * e^{j^*\boldsymbol{\mu}}, \tag{2}$$

where $\boldsymbol{E_{dB}} = 20 \times lg\boldsymbol{E}$ is the output pattern, and

$$\sigma = \boldsymbol{\sigma_{ideal}}(\theta_0,\phi_0) + \boldsymbol{\sigma_{error}} \tag{3}$$

is the near-field phase vector consisting of the phase values of the individual antenna elements, which can also be described as follows:

$$\sigma = [\sigma_1, \sigma_2, \ldots, \sigma_N], \tag{4}$$

where σ_k is the phase value of the kth element, θ is the azimuth angle, ϕ is the elevation angle, and $\boldsymbol{\mu}$ is the spatial transformation factor for the far field. N is the number of the PA elements.

The ideal phase of the antenna $\boldsymbol{\sigma_{ideal}}$ is decided only by the target steering angle(θ_0,ϕ_0):

$$\boldsymbol{\sigma_{ideal}}(\theta_0,\phi_0) = \left[\beta_{(1,1)}, \beta_{(1,2)}, \ldots, \beta_{(8,8)}\right] \tag{5}$$

where $\beta_{(m,n)}$ is the phase shift of the element in the n-column of the m-row and is calculated as follows:

$$\beta_{(m,n)} = -kd\sin\phi_0\left[(m-1)\cos\theta_0 + (n-1)\sin\theta_0\right], \tag{6}$$

where k is the wavenumber and d is the element gap.

As for the phase error $\boldsymbol{\sigma_{error}}$, it derives from several factors. For example, the nonideal power distribution network results in the initial phase imbalance of the microwave signal before passing the phase shifter. The phase shifters' inconsistent responses to the driven voltage lead to a phase distortion in the near-field. All these errors are random, and for the antenna used in the experiments,

https://doi.org/10.1017/S175907872400014X Published online by Cambridge University Press

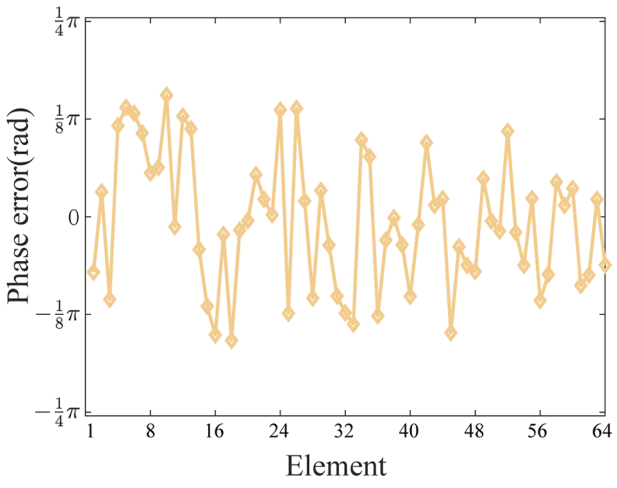

Figure 2. A set of phase errors applied to 64 elements.

its phase errors are within ±0.5 rad. Therefore, the applied phase error $\boldsymbol{\sigma_{error}}$ uniformly takes values over a range of −0.5 to 0.5 rad randomly (Fig. 2).

A comparison of LC-MPA's radiation patterns with and without phase errors is shown in Fig. 3, in which θ- and ϕ-cut of the far-field radiation patterns are presented. To evaluate the radiation pattern, beam efficiency, side-mode suppression ratio (SMSR), and main lobe gain were calculated. Beam efficiency is described as follows:

$$\eta = \frac{P_{main\ lobe}}{P_{total}}, \tag{7}$$

where $P_{main\ lobe}$ is the energy of the main lobe and P_{total} is the total energy of the far field.

SMSR is given as follows:

$$SMSR = \frac{P_{main\ lobe}}{P_{max\ side}}, \tag{8}$$

where $P_{max\ side}$ is the energy of the max side lobe.

The near-field phase errors resulted in considerable deterioration in the far-field, in which the beam efficiency of the radiation pattern with phase errors was reduced by approximately 3% and 16% in the azimuthal and elevational patterns, respectively. The SMSR of the θ-cut radiation pattern decreased around 3 dB, and the main lobe gain of both θ- and ϕ-cut of the far-field radiation patterns also reduced.

The dataset was generated using the simulation model. About 10,800 sets of patterns $\boldsymbol{E_{dB}}$ and the corresponding phase errors $\sigma_{\boldsymbol{error}}$ were obtained, of which 10,000 sets were set to deflect along the normal vector (0°). The other 800 were deflected by 0.05° for every 100 patterns to include the non-normal directions, as the main lobe may not precisely point to 0° in experiments. Here, the amplitude imbalance of each phase channel was not included in the dataset. This is because, for a phase-only modulation antenna, the phase imbalance dominates the deterioration of LC-MPA's radiation pattern compared to the amplitude imbalance. Besides, recent progress showed that even the NN model constructed without considering amplitude imbalance is able to cope with the imbalance up to about 1.4 dB [17].

Meanwhile, 100 sets of data for validation were generated. The pattern $E_{dB}(\theta, \phi)$ is an array of size 91 × 361, θ has a value of $(0, 360)$, ϕ has a value range of $(0, 90)$, both with angle step of 1. The training label is the phase error vector $\sigma_{\text{error}} = [\sigma_{error1}, \sigma_{error2}, \cdots, \sigma_{errorN}]$. Therefore, the dataset put into the NN for training consists of inputs of size $(10800, 91, 361)$ and labels of size $(10800, 64, 1)$.

NN construction

The schematic diagram of the constructed NN and its training and validation process are presented in Fig. 4. The NN is a fully connected network with 10 layers, and the number of nodes per layer is shown in Table 1.

In the training process, the training data, which is the radiation pattern, is input to the NN. The output is the calculated phase errors through the NN, which is used to compute the loss function with the training label, and the value of the loss function determines how the weights between nodes change. This process repeats, and the weights of the NN keep updating until the loss value declines to a certain value. In the validation process, the test data are put into the NN, which has completed training. The output is the estimated phase errors, which are then compared with the test label, calculating the estimation error.

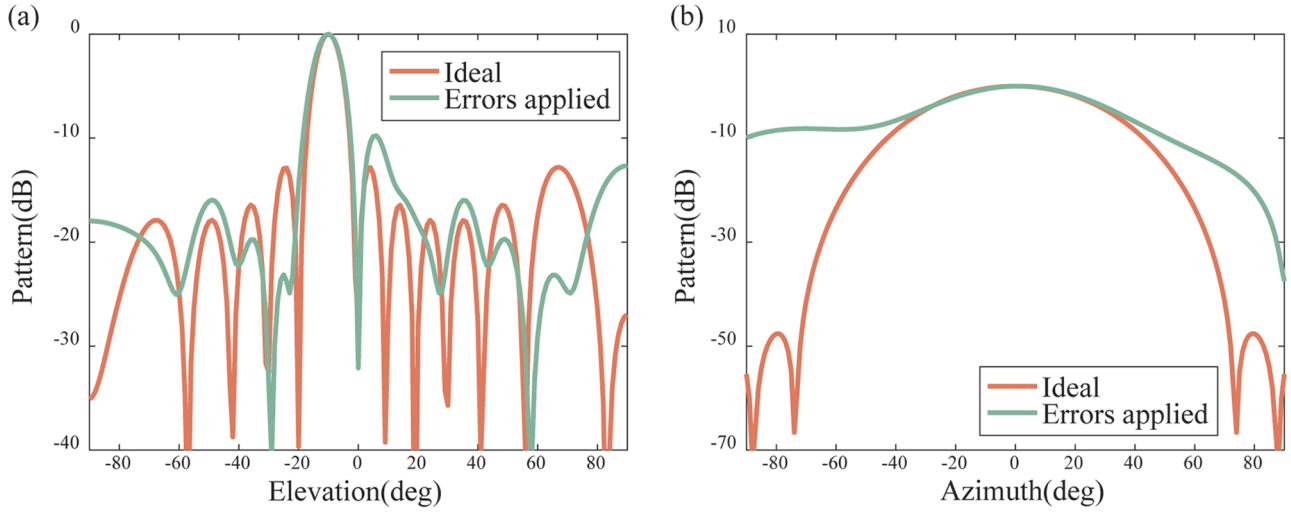

Figure 3. A comparison of the far-field radiation patterns before and after applying phase errors: (a) ϕ-cut (b) θ-cut.

https://doi.org/10.1017/S1759078724000014X Published online by Cambridge University Press

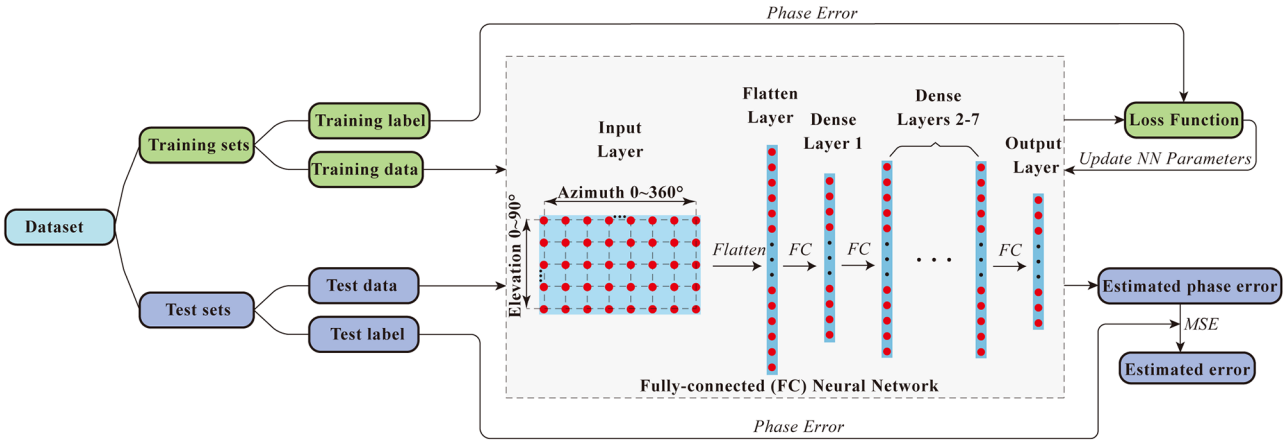

Figure 4. Schematic diagram of the NN along with its training and validation process.

Table 1. Structure of the NN

Layer (type)	Output shape
Input layer	(91, 361)
Flatten	(32,851)
Dense 1	(361)
Dense 2	(3000)
Dense 3	(3000)
Dense 4	(3000)
Dense 5	(3000)
Dense 6	(3000)
Dense 7	(3000)
Output layer	(64)

Table 2. Parameters of the NN

Parameter	Output shape
Activation function in dense layers	ReLU
Initial learning rate	1e-5
Number of training epochs	350
Decay rate of learning rate	0.99
Optimizer	Adam
Loss function	MSE
Batch size	100

The activation function used in dense layers is the rectified linear unit (ReLU) function, and the loss function is the mean square error (MSE), which is given as follows:

$$\delta_{MSE} = \frac{\sum_{i=1}^{N} (\hat{\sigma}_{error\ i} - \sigma_{error\ i})^2}{N} \quad (9)$$

where $\hat{\sigma}_{error\ i}$ is the predicted phase error of the ith element and $\sigma_{error\ i}$ is the actual phase error. The MSE function is used in the validation process as well, and the value of this function is the estimated error.

A detailed parameter configuration is presented in Table 2. After 350 epochs, training loss converged at 4.5e−3. The trained NN is considered a phase error estimation model.

Phase calibration method

There are two parts to the phase calibration method, calibration and compensation process, as illustrated in Fig. 5. In the calibration process, nine characteristic patterns were obtained initially, all steering at the normal vector but driven with different specific control voltages. These voltages correspond to phases from 0 to 2π, stepping by $\frac{\pi}{4}$. The smaller the phase step is set, the more patterns will be tested to offer more precise error information, yet with more time consumption. Practically, a trade-off between precision and speed is required. After several tries, nine measurements were set as an empirical value, which is the smallest number of patterns that maintains the precision of calibration. Then, the relation between voltages and phase was given by a curve truncated from the original voltage–phase curve (also called the "u-phi curve") (Fig. 6), which was obtained by testing a single phase shifter identical to the phase shifters in the antenna used in the experiment. To leave space for subsequent voltage adjustment, the truncation did not start at both ends of the original curve but in a range of relatively linear curves with 2π phase retardation.

The measured characteristic radiation patterns were then put into the phase error estimation model, and the estimated phase errors of each element at specific voltages were obtained. Hence, a voltage–phase error curve for every element was fitted, in which two fitting methods were applied (Fig. 7), interpolation and linear fitting. Voltage–phase error curves for all elements were combined to become a PA calibration file used in the compensation process. With a desired steering angle, the compensation for each element's phase error was obtained from the file by indexing the location of the element and the uncalibrated voltage. By subtracting the estimated phase errors, the compensated phase and the corresponding calibrated control voltages were obtained, which were then applied to the antenna. Both optimized and unoptimized control voltages were applied to compare the performance of the proposed calibration method.

Simulation and experimental verification

Simulation results

Simulation results for the phase error estimation model validation are shown in Fig. 8. Radiation patterns in the validation

https://doi.org/10.1017/S1759078724000014X Published online by Cambridge University Press

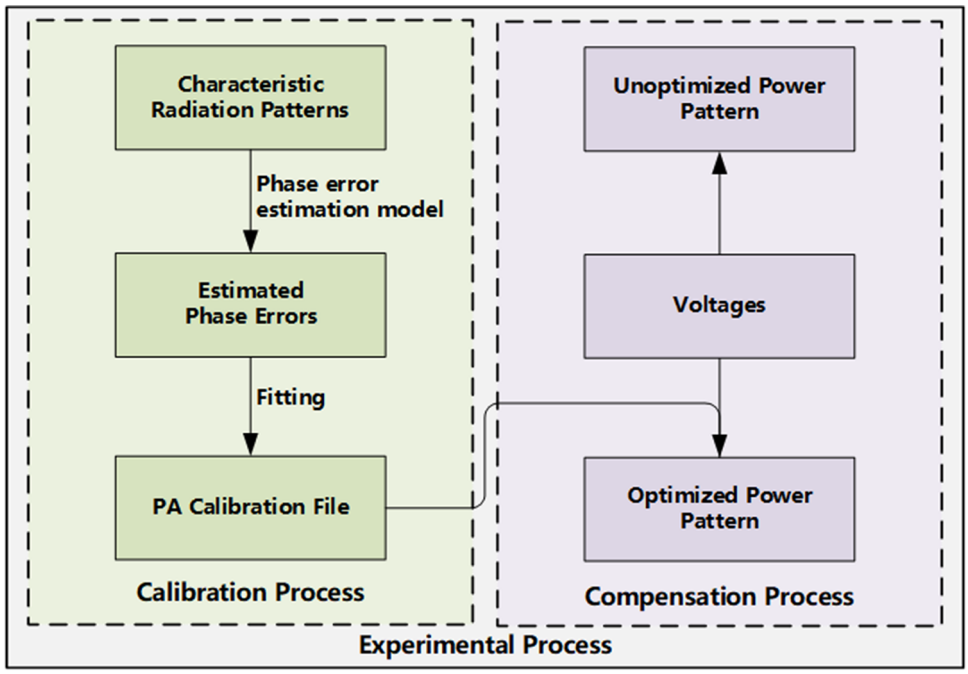

Figure 5. Flow chart of the proposed LC-MPA calibration method.

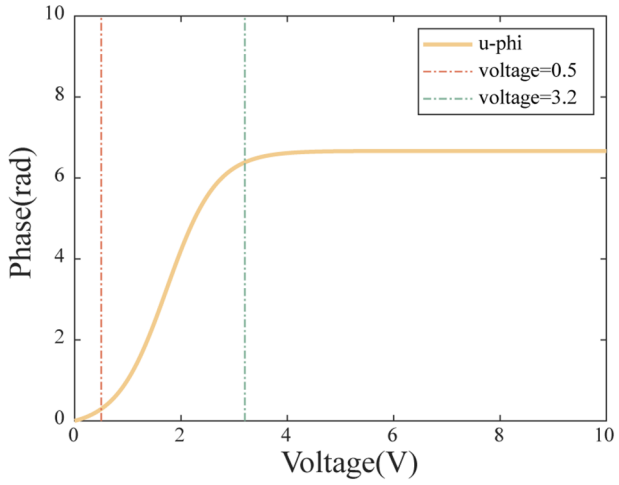

Figure 6. Voltage–phase relation curve of an LC-MPA.

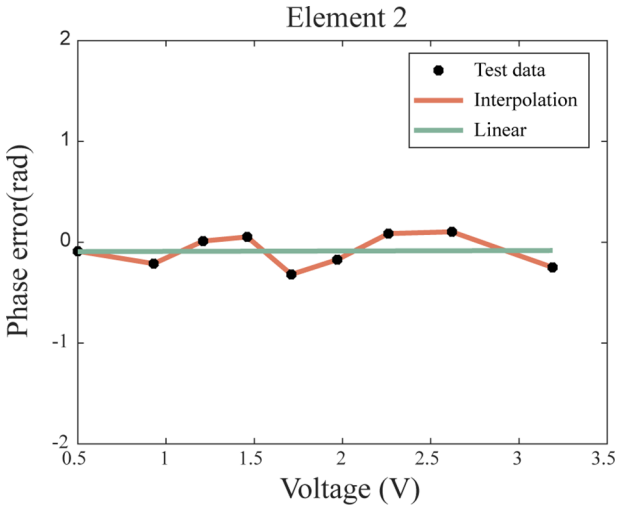

Figure 7. Fitting voltage–phase error curves for the second element.

dataset were put into the estimation model to obtain their predicted phase errors. The predicted phase errors are compared with those in the validation dataset, and their corresponding radiation patterns are compared as well. The average case of δ_{MSE} is shown in Fig. 8(a, b), and the worst case is shown in Fig. 8(c, d). The average phase estimation error δ_{MSE} is 3.9e−3 (approximately 3.58°), and the worst is 1.1e−2 (approximately 6°), which are comparable with the results in previous works [17, 24].

To demonstrate the precision of the proposed phase calibration method, another simulation was conducted. In the simulation, a simulated LC-MPA antenna was constructed first. Each element of the simulated antenna was applied a phase error over a range of −0.5 to 0.5 rad randomly and an extra phase error over a range of −0.1 to 0.1 rad, which changed with different driven voltages. Through carrying out the described experiment process, calibrated radiation patterns were obtained, including the one using the interpolation fitting method and the one using the linear fitting method, which are shown in Fig. 9. In addition, radiation power patterns generated by the uncalibrated phases, the ideal phases, and the calibrated phases obtained by applying the SPGD method are also demonstrated. Here, the ideal radiation patterns set a benchmark for MPA optimization and can be used to evaluate the quality of the calibrated patterns. The difference between linear and interpolation calibrated patterns is negligible, due to the linearity of the u-phi curve of the antenna used in the simulation and the subsequent experiments.

Figure 10 shows the root of mean square errors (RMSE) between the SPGD calibrated pattern and the ideal pattern, which

https://doi.org/10.1017/S175907872400014X Published online by Cambridge University Press

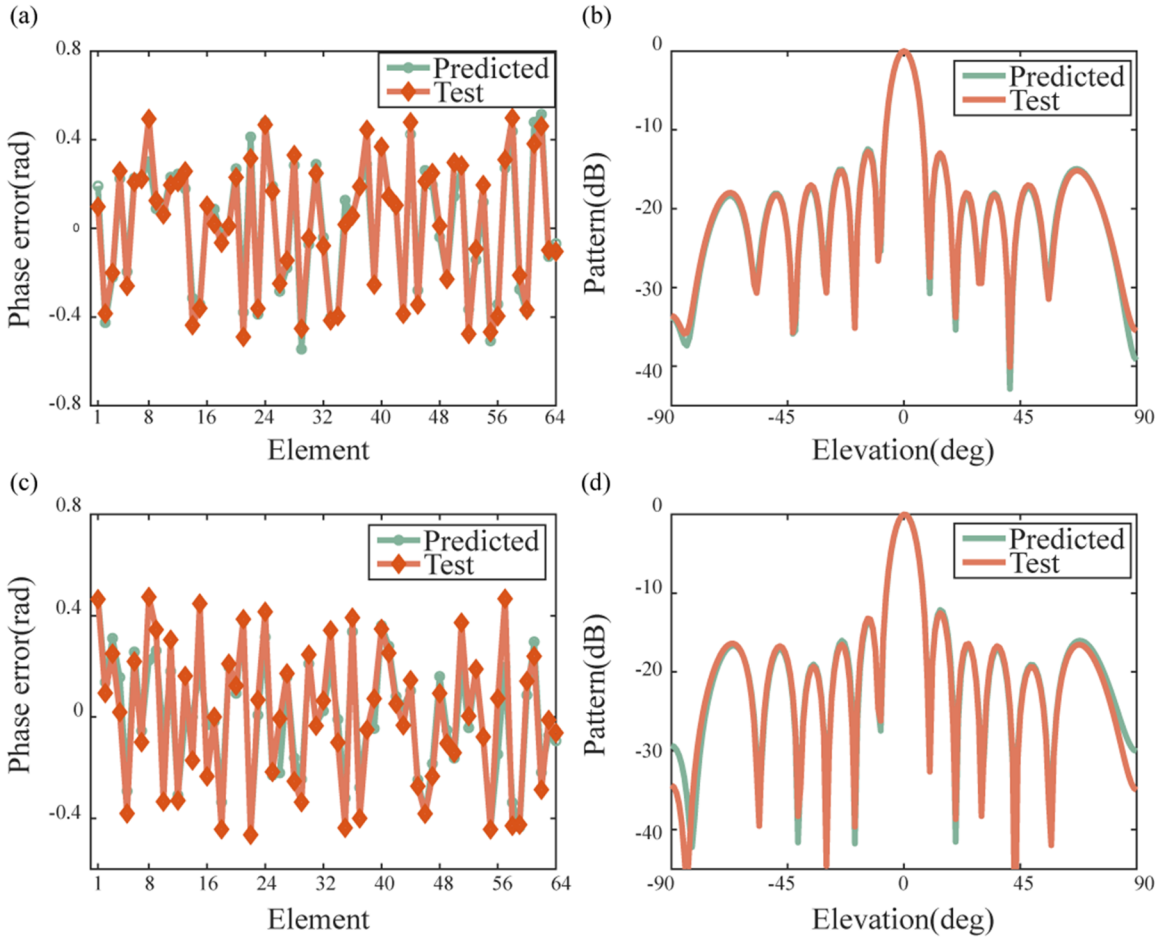

Figure 8. Simulation validation results. Comparisons of (a) near-field phase error distributions and (b) far-field radiation patterns in the average case of δ_{MSE}; (c) and (d) Comparisons in the worst case of δ_{MSE}.

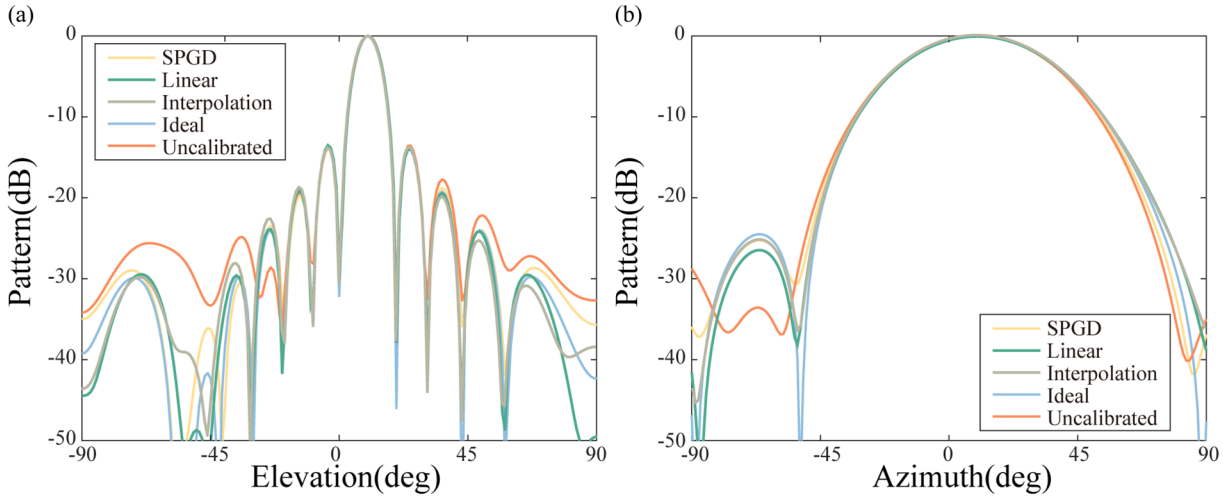

Figure 9. Simulation results: comparison of radiation power patterns generated by ideal, uncalibrated, and calibrated phases. The calibrated phases are obtained by applying SPGD and the proposed fast phase calibration method: (a) ϕ-cut (b) θ-cut.

converges at approximately 7.5°. The calibrated patterns obtained by applying SPGD have a similar quality to the results obtained by applying the proposed method, but it takes more than 4,000 iterations to reach convergence, which is impractical in experiments due to LC-MPA's slow response speed. Compared to thousands of iterations, the proposed method is more time-saving with only several measurements and offers comparable optimization performances.

https://doi.org/10.1017/S1759078724000014X Published online by Cambridge University Press

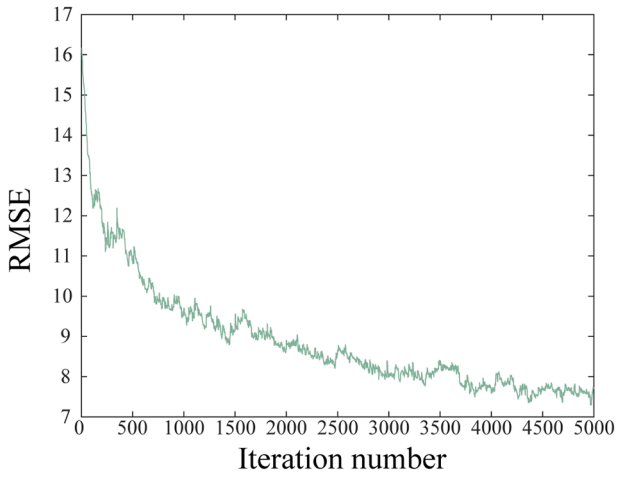

Figure 10. The RMSE curve of LC-MPA phase calibration by SPGD.

Experiment

The experimental setup is shown in Fig. 11. The PC was used to send the control signals, the voltage code, to the circuit board, which links to the antenna via FPC, applying voltages to every element separately. The vector network analyzer provided excitation to the antenna, and the probe in the anechoic chamber, which was set to be approximately six times the wavelength away from the antenna, scanned an area containing 41 × 41 scanning points and measured the radiation signal. This measured data were then transmitted to the vector network analyzer for analysis and calculated to convert to the radiation power patterns.

Experiments at different steering angles were conducted to verify the calibration method. The experimental results are shown in Fig. 12, in which both θ- and ϕ-cut of the radiation patterns are presented.

In Fig. 12, there are two radiation power patterns in each figure, the uncalibrated pattern with the original voltages applied, and the calibrated pattern using the NN-adjusted driven voltages. Overall, the LC-MPA's deflection performance at different angles was improved. The deflection efficiency of the $\phi = 6^\circ$, 12°, and -20° azimuth patterns increased by approximately 9%, 4%, and 6%, respectively, and all of the SMSRs increased by around 2 dB. For the elevation patterns, it can be seen that with the increase of deflection angles, the radiation power patterns had a more considerable improvement. This is because the deflection efficiency of the antenna decreases drastically at large elevation angles, which allows for a greater potential for optimization. The efficiency of the $\theta = 6^\circ$ and 12° elevation patterns slightly improved by 1–2.5%, whereas $\theta = -20^\circ$ saw considerable increases in efficiency by 10%, the SMSR by 4 dB, and the main lobe gain by 2 dB, which are comparable with the state-of-the-art LC-MPAs [4].

Conclusion

In this paper, a fast phase calibration method was proposed to optimize the deflection performance of LC-MPAs. First, an antenna simulation model was built to generate a dataset of radiation patterns and phase errors. Then, the phase error estimation model was obtained by training the NN with the simulated dataset. After inputting several measured characteristic radiation patterns into the estimation model, the estimated phase errors for each antenna element at several driven voltages were obtained, which then became the PA calibration files. The PA calibration file provided phase errors for each antenna element at different driven voltages and was then used for the LC-MPA's phase calibration and deflection performance optimization. At last, simulations and experiments on a 64-channel, two-dimensional planar LC-MPA were conducted to verify this method.

Results show that the method offered precise phase estimation with an average error of 3.58°, realized a fast calibration process with only several field-measured radiation patterns and improved the performances of the LC-MPA by approximately 4–10% in deflection efficiency at different steering angles. This method provided a viable approach to calibrate the LC-MPAs within only several in-situ measured patterns, laying a foundation for applications. Further improvement to the proposed method

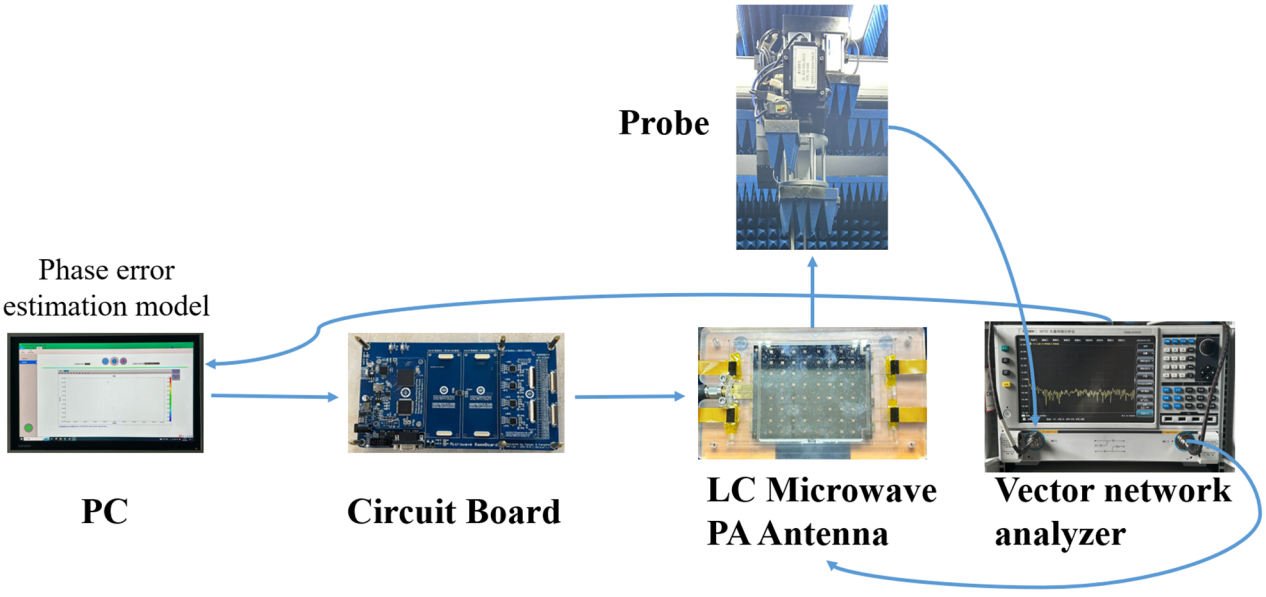

Figure 11. Diagram of the experimental setup.

https://doi.org/10.1017/S175907872400014X Published online by Cambridge University Press

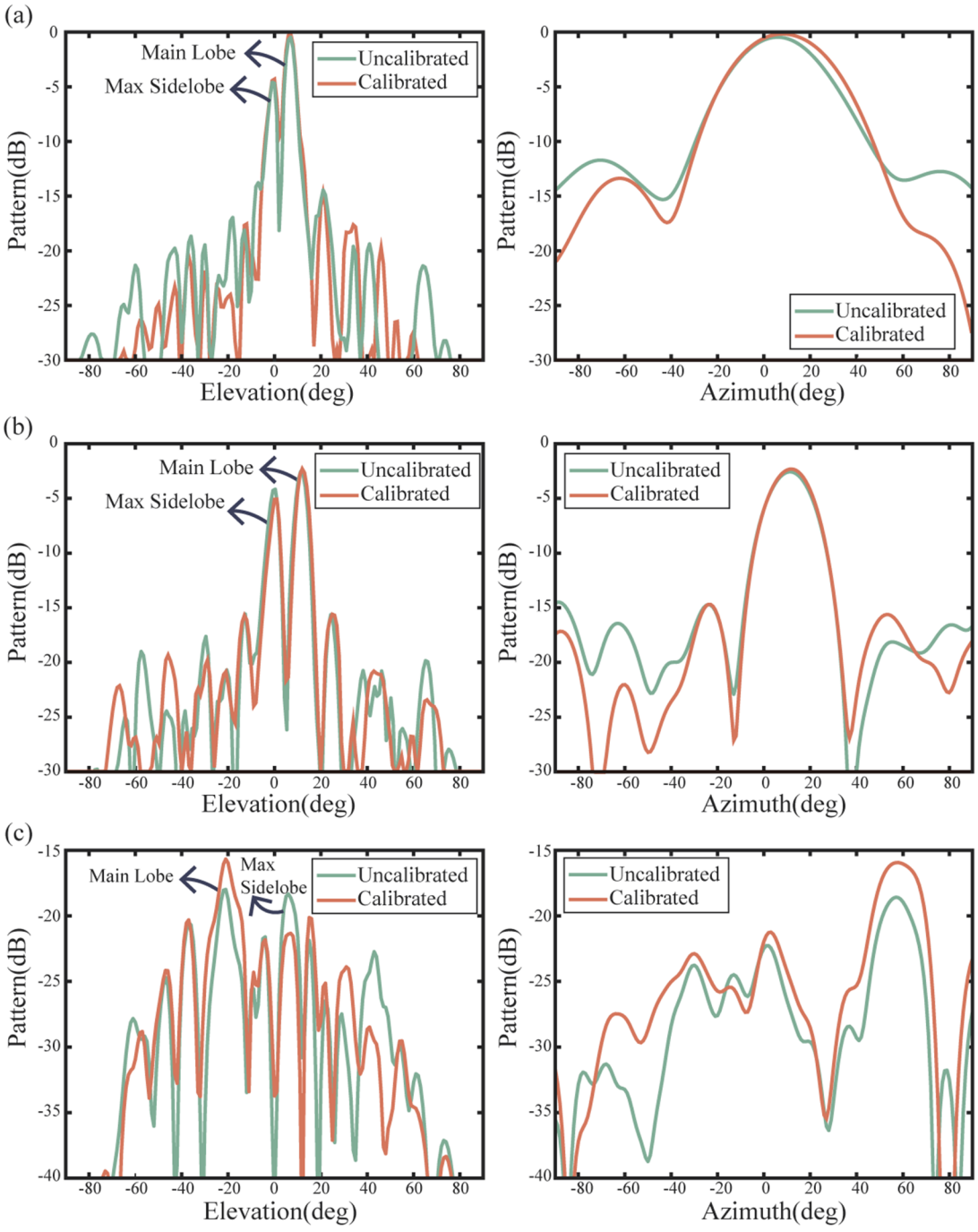

Figure 12. Experiment results of far-field radiation patterns deflected at different angles: (a) ϕ- and θ-cut patterns at $\phi = 6^\circ$, $\theta = 6^\circ$; (b) $\phi = 12^\circ$, $\theta = 12^\circ$; (c) $\phi = -20^\circ$, $\theta = 60^\circ$.

may include enhancing the accuracy of the phase error estimation model by increasing the categories of phase errors in the dataset and conducting a second-stage NN training using the measured characteristic patterns.

Funding statement. This work is sponsored by the Key-Area Research and Development Program of Guangdong Province (2019B010158001), the National Natural Science Foundation of China (61871031), the Department of Science and Technology of Shandong Province (2021TSGC1043), and the National Key Research and Development Program of China (2018YFA0307400).

Competing interests. The authors report no conflict of interest.

References

1. **Parker D and Zimmermann DC** (2002) Phased arrays – part 1: Theory and architectures. *IEEE Transactions on Microwave Theory & Techniques* **50**(3), 678–687.
2. **Stark L** (1974) Microwave theory of phased-array antennas – A review. *Proceedings of the IEEE* **62**(12), 1661–1701.
3. **Wang Y, Wang X, Wang Y, Yu C, Zhang W, Liang F, Zhang Z, Gao S and Chen J** (2020) Reconfigurable microwave phase shifter based on

https://doi.org/10.1017/S175907872400014X Published online by Cambridge University Press

nematic liquid crystal: Design and experimental validation. In *2020 IEEE 3rd International Conference on Electronic Information and Communication Technology (ICEICT)*, 455–459.
4. **Zhang W, Li Y and Zhang Z** (2022) A reconfigurable reflectarray antenna with an 8 μm-thick layer of liquid crystal. *IEEE Transactions on Antennas and Propagation* **70**(4), 2770–2778.
5. **Resler DP, Hobbs DS, Sharp RC, Friedman LJ and Dorschner TA** (1996) High-efficiency liquid-crystal optical phased-array beam steering. *Optics Letters* **21**, 689–691.
6. **Winker B, Mahajan M and Hunwardsen M** (2004) Liquid crystal beam directors for airborne free-space optical communications. In *2004 IEEE Aerospace Conference Proceedings (IEEE Cat. No. 04TH8720)*, vol 3. Big Sky, MT, USA, 1709.
7. **McManamon PF, Bos PJ, Escuti MJ, Heikenfeld J, Serati S, Xie H and Watson EA** (2009) A review of phased array steering for narrow-band electrooptical systems. *Proceedings of the IEEE* **97**(6), 1078–1096.
8. **Reese R, Polat E, Tesmer H, Strobl J, Schuster C, Nickel M, Granja AB, Jakoby R and Maune H** (2019) Liquid crystal based dielectric waveguide phase shifters for phased arrays at W-band. *IEEE Access* **7**, 127032–127041.
9. **Rosaline I, Kumar A, Upadhyay P and Murshed AH** (2022) Four element MIMO antenna systems with decoupling lines for high-speed 5G wireless data communication. *International Journal of Antennas and Propagation* **2022**, 1–13.
10. **Chaturvedi D and Kumar A** (2023) A QMSIW cavity-backed self-diplexing antenna with tunable resonant frequency using CSRR slot. *IEEE Antennas and Wireless Propagation Letters* **23**(1), 259–263.
11. **Jwair MH and Elwi TA** (2023) Steerable composite right–left-hand-based printed antenna circuitry for 5G applications. *Microwave and Optical Technology Letters* **65**(7), 2084–2091.
12. **Ismail MM, Elwi TA and Salim AJ** (2023) Reconfigurable CRLH-inspired antenna based on Hilbert curve EBG structure for modern wireless systems. *Microwave and Optical Technology Letters* **65**, 2646–2655.
13. **Vorontsov MA, Carhart GW and Ricklin JC** (1997) Adaptive phase-distortion correction based on parallel gradient-descent optimization. *Optics Letters* **22**, 907–909.
14. **Boeringer DW and Werner DH** (2004) Particle swarm optimization versus genetic algorithms for phased array synthesis. *IEEE Transactions on Antennas and Propagation* **52**(3), 771–779.
15. **Keen-Keong Y and Yilong L** (1997) Sidelobe reduction in array-pattern synthesis using genetic algorithm. *IEEE Transactions on Antennas and Propagation* **45**(7), 1117–1122.
16. **Cao Z, Zhang X, Osnabrugge G, Li J, Vellekoop IM and Koonen AMJ** (2019) Reconfigurable beam system for non-line-of-sight free-space optical communication. *Light: Science & Applications* **8**, 69.
17. **Iye T, Van Wyk P, Matsumoto T, Susukida Y, Takaya S and Fujii Y** (2022) Neural network-based phase estimation for antenna array using radiation power pattern. *IEEE Antennas and Wireless Propagation Letters* **21**(7), 1348–1352.
18. **LeCun Y, Bengio Y and Hinton G** (2015) Deep learning. *Nature* **521**(7553), 436–444.
19. **Sallam T, Abdel-Rahman AB, Alghoniemy M, Kawasaki Z and Ushio T** (2016) A neural-network-based beamformer for phased array weather radar. *IEEE Transactions on Geoscience and Remote Sensing* **54**(9), 5095–5104.
20. **Shrestha S, Fu X and Hong M** Optimal solutions for joint beamforming and antenna selection: From branch and bound to machine learning. doi:10.48550/arXiv.2206.05576
21. **Kim JH and Choi SW** (2020) A deep learning-based approach for radiation pattern synthesis of an array antenna. *IEEE Access* **8**, 226059–226063.
22. **Liu J, Liang F and Wang B-Z** (2022) 2-D beam scanning broadband reflectarray antenna with low thickness of liquid crystal. In *2022 IEEE Conference on Antenna Measurements and Applications (CAMA)*, Guangzhou, China, 1–4.
23. **Weil C, Luessem G and Jakoby R** (2002) Tunable inverted-microstrip phase shifter device using nematic liquid crystals. In *2002 IEEE MTT-S International Microwave Symposium Digest (Cat. No.02CH37278)*, vol 1, Seattle, WA, USA, 367–371.
24. **Leng L, Zeng Z, Wu G, Lin Z, Ji X, Shi Z and Jiang W** (2022) Phase calibration for integrated optical phased arrays using artificial neural network with resolved phase ambiguity. *Photonics Research* **10**(2), 347–356.

Qianying Yan is currently an undergraduate student majoring in information engineering at the University of Electronic Science and Technology of China (UESTC). Her current research interests include liquid crystal microwave antennas and machine learning.

Yanwei Huang received his B.E. degree from Southwest Jiaotong University in 2020. He is pursuing a Master's degree in optical engineering at the University of Electronic Science and Technology of China (UESTC). His current research interests include liquid crystal optical phased array and microwave antennas.

Wenzhao Zhang received his B.E. degree from the University of Electronic Science and Technology of China (UESTC) in 2020. Currently, he is pursuing a master's degree in optical engineering at the UESTC. His current research interests include liquid crystal microwave antennas.

Xin Hou is currently a graduate student majoring in optical engineering at the University of Electronic Science and Technology of China. His current research interests include liquid crystal phased array antennas and beam control systems.

Mengqing Zhang received her bachelor's degree from Jinan University in 2021. She is pursuing a master's degree in optical engineering at the University of Electronic Science and Technology of China (UESTC). Her current research interests include liquid crystal microwave phased array antennas and polymer network liquid crystals.

https://doi.org/10.1017/S175907872400014X Published online by Cambridge University Press

Xiangru Wang received his B.E. and PhD degrees from the University of Electronic Science and Technology of China (UESTC). He is a professor at the School of Optoelectronic Information, UESTC. His current research interests include free-space optical communications, optical phased array, and reconfigurable microwave antennas.

Feng Liang was born in Hubei, China, in 1983. He earned his B.S. degree in applied physics from the University of Electronic Science and Technology of China (UESTC) in Chengdu, China, in 2006, and his Ph.D. in electrical engineering from Wuhan University in Wuhan, China, in 2011. Since July 2011, he has been a faculty member at UESTC, where he currently serves as a professor. His research interests include the theory and implementation of controlling electromagnetic fields and waves.

https://doi.org/10.1017/S175907872400014X Published online by Cambridge University Press